Quantum Well Devices for

Photonic Networks

Final Progress Report

October 15, 1999

U. S. Army Research Office

DAAG55-97-1-0002

Stanford University

Approved for Public Release

Distribution Unlimited

1   **20000628 057**

REPORT DOCUMENTATION PAGE

1. AGENCY USE ONLY *(Leave blank)*	2. REPORT DATE	3. REPORT TYPE AND DATES COVERED
		Final Report

4. TITLE AND SUBTITLE	5. FUNDING NUMBERS
Quantum Well Devices for Photonic Networks	
6. AUTHOR(S) James S. Harris	DAAG55-97-1-0002

7. PERFORMING ORGANIZATION NAMES(S) AND ADDRESS(ES)	8. PERFORMING ORGANIZATION REPORT NUMBER
Stanford University Stanford, CA 04305	

9. SPONSORING / MONITORING AGENCY NAME(S) AND ADDRESS(ES)	10. SPONSORING / MONITORING AGENCY REPORT NUMBER
U.S. Army Research Office P.O. Box 12211 Research Triangle Park, NC 27709-2211	ARO 35564.1-EL

11. SUPPLEMENTARY NOTES

The views, opinions and/or findings contained in this report are those of the author(s) and should not be construed as an official Department of the Army position, policy or decision, unless so designated by other documentation.

12a. DISTRIBUTION / AVAILABILITY STATEMENT	12 b. DISTRIBUTION CODE
Approved for public release; distribution unlimited.	

13. ABSTRACT *(Maximum 200 words)*

The first part of this report discusses a X-modulator, a powerful device in terms of optical computation, routing, and interconnection. The device is a 3 input, 3 output conservative and reversible switch, an optoelectronic Fredkin gate. Using arrays of these modulators, various reconfigurable switching, routing, and interconnection networks are constructed.

The second part of this report discusses the high speed properties of vertical cavity modulators for optical interconnection and switching. The epitaxial structure, mask design, device processing and characterization of high speed vertical cavity resonant enhanced MQW modulators is described.

14. SUBJECT TERMS	15. NUMBER IF PAGES
	16. PRICE CODE

17. SECURITY CLASSIFICATION OR REPORT	18. SECURITY CLASSIFICATION OF THIS PAGE	19. SECURITY CLASSIFICATION OF ABSTRACT	20. LIMITATION OF ABSTRACT
UNCLASSIFIED	UNCLASSIFIED	UNCLASSIFIED	UL

Chapter 1—Introduction

Quantum well optoelectronic devices are important components for high-performance photonic communication and interconnection systems. Vertical cavity modulators grown by molecular beam epitaxy have several characteristics which make them desirable from a systems standpoint, including low power dissipation, high speed, large contrast ratio, high bandwidth, the ability to fabricate dense arrays, integration with GaAs and silicon VLSI, and a wide range of wavelengths of operation (for WDM).

The first part of this report discusses a X-modulator developed at Stanford. This is a very powerful device in terms of optical computation, routing, and interconnection. The device is essentially a 3 input, 3 output conservative and reversible switch, an optoelectronic implementation of a Fredkin gate. The use of these devices for optical logic is exhibited and an implementation of a full adder using only 5 devices is shown. Using arrays of these modulators, various reconfigurable switching, routing, and interconnection networks are constructed, including crossbar switches and field programmable gate arrays. Ongoing research with these devices is focussed on improving their characteristics and making them more flexible for use in systems applications. In particular, reduced operating voltages are obtained using graded buffer layer techniques, methods for optically controlling the devices are examined, and gain layers are incorporated into these structures to compensate for the losses involved in cascading the devices.

The second part of this report discuss the high speed properties of vertical cavity multiple quantum well modulators for optical interconnection and switching. The high speed device consists of the top and bottom DBR mirrors made of $Al_{0.35}Ga_{0.65}As/AlAs$, the undoped regions between top and bottom inter cavity contacts contain quantum wells. This device offers high on-off contrast, low operating voltage swing, low insertion loss and can easily to be integrated with silicon electronics. The wavelength selectivity and high speed response of these devices make them ideal for dense wavelength division multiplexing(DWDM) applications. We discuss in detail the epitaxial structure, mask

2

and characterization of these high speed vertical cavity resonant enhanced MQW modulators.

Finally, a new class of optoelectronic devices which can be evanescently coupled to single-mode optical fibers is described. Traditionally, the processing of fiber-optic signals involves the interruption of the fiber and coupling of the optical signal into and out of an electro-optic component. There are several disadvantages associated with this approach, including high-insertion loss, mechanical instability and high packaging costs. Semiconductor in-line fiber devices, in which light is evanescently coupled between single mode fibers and multimode semiconductor waveguides, offer solutions to these problems. The issues associated with the design and implementation of such devices are examined in detail.

Chapter 2--X-Modulator

2.0 Introduction

To perform extremely efficient optical switching, routing, and logic, photonic switches and gates should ideally be conservative (preserving optical input power) and reversible (inputs and outputs can be interchanged). Such a device forms a natural and complete primitive for decomposing logic functions. The transmission reflection modulators we have developed (hereby known as X-modulators) when used as an X-gate (inputs on both sides of the device), or as a single device controllable exchange function—an exchange bypass or 2x2 switch (Figure 2-1).
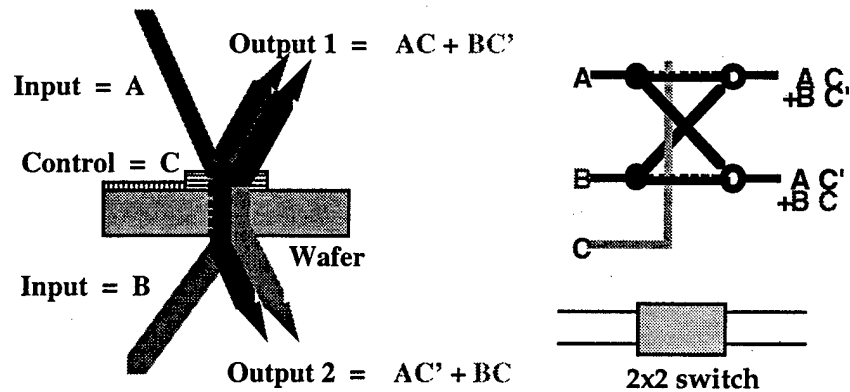
Figure 2-1: Conceptual representations of the X-modulator

The X-gate's current implementation is electro-optical, with one electrical control and two optical data inputs. It is the logical implementation of a Fredkin gate (3-input, 3-output conservative, reversible gate). Logic that is conservative and reversible can have very low power dissipation, in that it conserves the number of 1's in the input and output. The reversibility of the gate increases its architectural functionality. These devices are essentially controllable optical routing elements, mirrors, or beamsplitters. In one state beams incident from opposite sides of the device are reflected and in the other state they are transmitted or cross each other. Using arrays of these devices, various switching networks can be constructed, including crossbar switches and other regular or irregular 2-D or 3-D architectures. This chapter will describe the basics of conservative invertible logic, discuss the X-modulator device design, describe several potential systems applications of the device including optical logic and interconnection, and finally describe some refinements to the initial device design that make it more amenable to systems applications.

2.1 Conservative Invertible Logic

Conservative and invertible (CI) logic is defined as follows--an n-input n-output Boolean function f is said to be conservative and invertible if it satisfies the following conditions:

- $B^n \rightarrow B^n$ is bijective, where $B=\{0,1\}$
- For any input vector x, $w(x)=w(f(x))$ where

4

$$w[x]=w[(x_1,x_2,...x_n)]=\Sigma^n_{i=1}x_i.$$

The first condition represents the invertibility of the function. There is a unique mapping between the inputs and the outputs and vice versa, so that the inputs may be determined given the outputs. The second condition describes the conservative aspect of the function. What it implies is that the number of 1's in the output is the same as that of the input. Figure 2-2 shows the truth table for one such 3 input-3 output CI function, namely the X-gate whose optoelectronic realization is the focus of this chapter.

Input a b c	Output d e f	
0 0 0	0 0 0	$d=ac'+bc$
0 0 1	0 0 1	
0 1 0	0 1 0	$e=ac+bc'$
0 1 1	1 0 1	
1 0 0	1 0 0	$f=c$
1 0 1	0 1 1	
1 1 0	1 1 0	
1 1 1	1 1 1	

Figure 2-2: Truth table of X-gate

By counting arguments, one can compute that there are a total of only 36 possible 3-input 3-output CI functions. These functions fall into six equivalent classes with respect to permutations of the output. The six representative functions of these classes are the X (x input conditionally switches y and z), Y (y controls), Z (z controls), R (right rotation), L (left rotation), and I (identity) gates. Furthermore, there are only three equivalent classes with respect to input and output permutation. The representative gates are X (for Y and Z), R (with L), and I. The X-gate and the R-gate are also individually logically complete, meaning that any Boolean function may be realized by some combination of several X-gates or several R-gates. In addition to this fact, they are universal in that using some cascade connections of X-gates with wire permutations can realize any 3-3 CI function. Figure 2-3 demonstrates how several common Boolean functions may be realized using X-gates and also includes the logic functions for X- and R-gates.
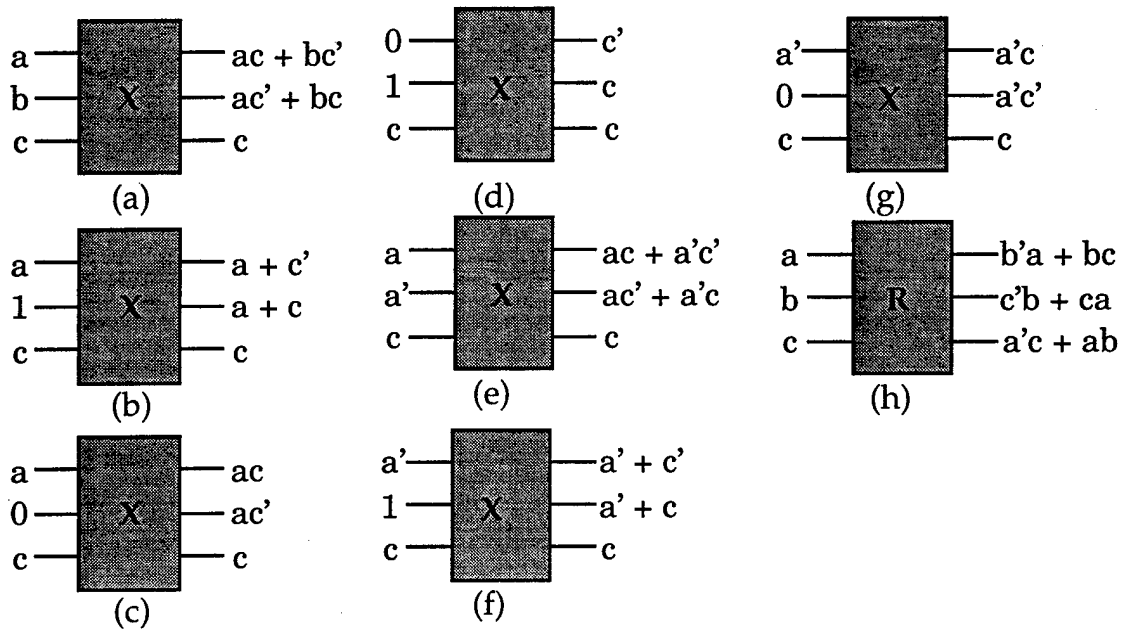
5

Figure 2-3: Common Boolean functions using X-gates (a-g) and the R-gate(h): a) X-gate, b) OR gate, c) AND gate, d) NOT gate or fanout, e) XOR gate, f) NOR gate, g) NAND gate, h) R-gate.

An important aspect of CI logic readily apparent from this figure is that it is often necessary to insert additional constants or sources at the input of a gate or function and that there are frequently extra signals at the output which may or may not be useful for further computation. As an example of this, note that part d of the figure implements both a 1-2 fan-out of the signal and generates its inverse. Figure 2-4 demonstrates how X-gates can be used to construct Y, Z, L, or R-gates. Note that for the Y and Z gates a simple permutation of inputs is sufficient, whereas for the R and L gate two X-gates are required. It is also possible to realize logic functions using R-gates, as well as constructing X,Y,Z, and L-gates with R-gates. In this case it is interesting to note that it takes 4 R-gates to realize an X-gate (only two were required for the reverse mapping). Figure 2-5 shows how an X-gate may be realized using R-gates.
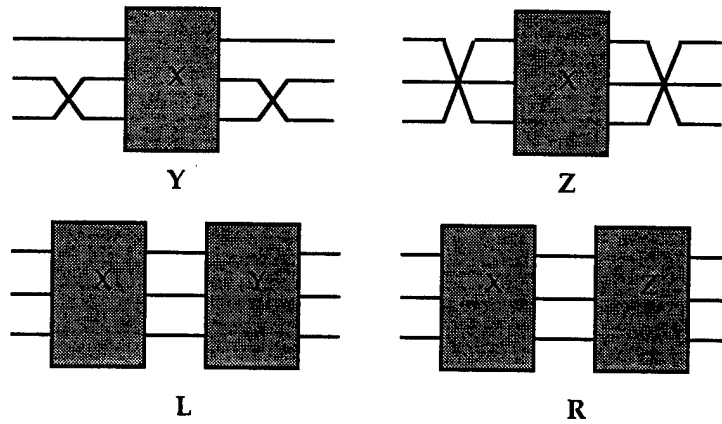
Figure 2-4: Universality of X-gate, demonstrating its use in constructing other 3-3 CI functions (Y, Z, L, and R-gates).
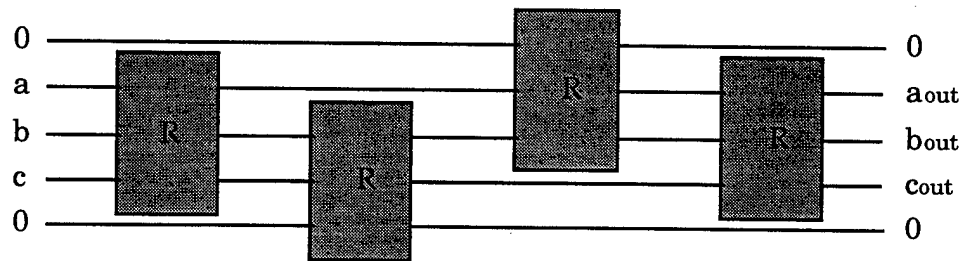

Figure 2-5: Construction of X-gate using 4 R-gates.

Because these X-gate type switches can perform logic functions, it is quite natural to construct a full adder from them, as we have done for Boolean logic and threshold logic with SEEDs. This full adder is shown in Figure 2-7. A program has been written in Mathematica to synthesize logic functions using X-gates. While we have shown how typical Boolean functions may be implemented using X-gates, a direct mapping of combinational logic onto X-gate logic is typically not the most efficient design in terms of number of devices.

7

Input	Output
a b c	d e f
0 0 0	0 0 0
0 0 1	0 0 1
0 1 0	0 1 0
0 1 1	1 0 1
1 0 0	1 0 0
1 0 1	1 1 0
1 1 0	0 1 1
1 1 1	1 1 1

a —— [R] —— d=b'a + bc
b —— [R] —— e=c'b + ca
c —— [R] —— f=a'c + ab
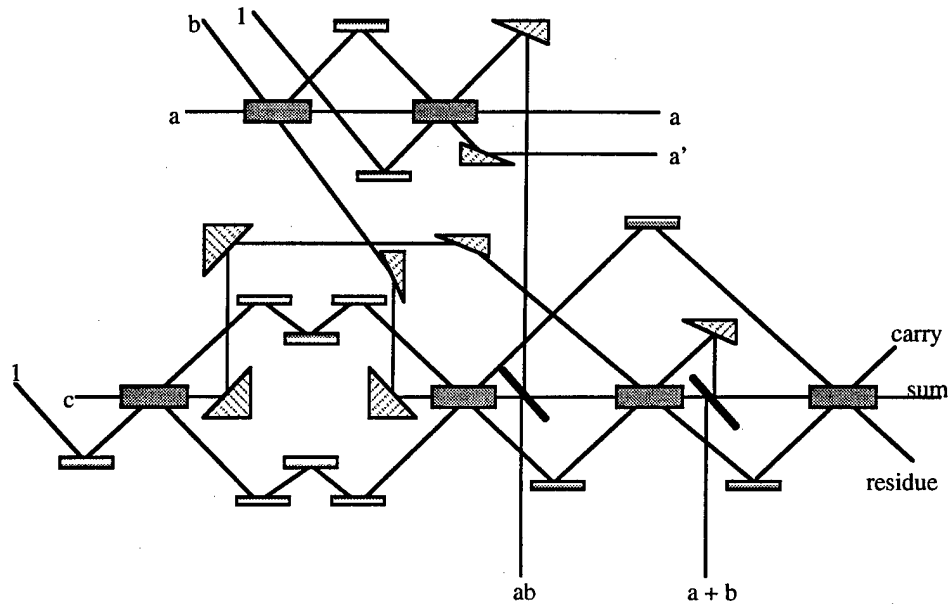
(h)

Figure 2-6: Truth table of R-gate.

Figure 2-7: Optical implementation of a full adder using CI X-gates

2.2 Previous Optical Implementations

There have been several optical implementations of Fredkin gates prior to the quantum well modulator based gate as described by Shamir et. al.: the polarization switching gate, acoustooptic gate, photorefractive gate, and waveguide or coupler switch. In a polarization switching gate, two orthogonal polarizations of light impinge upon an electrooptic modulator which rotates polarizations by 90 degrees when active. The control signal for this modulator may be either an electrical signal or an optical signal converted to

8

an electrical one by a photodetector. Both beams share the same physical path and can be separated by a polarizing beam splitter if necessary. In an acoustooptic gate, two laser beams are incident upon an acoustooptic deflector at the Bragg angle. If the acoustic control signal is present each beam is deflected into the other channel.

Photorefractive gates are based on four-wave mixing so that two control (or pump) beams when present will phase conjugate the two input signals thus switching the outputs. Perhaps the most promising of these four implementations is the modulated waveguide or fiber coupler which may be either electrically controlled or use an orthogonally polarized control signal to activate the coupling region (consisting of some nonlinear or electrooptic material) between the two inputs.

2.3 Device Design and Theory

The structure of the X-modulator consists of a slightly asymmetric Fabry-Perot cavity containing top and bottom mirrors of 10 and 12.5 periods of GaAs/AlAs quarter wave stacks surrounding an undoped cavity of 48, 75 Å $In_{0.2}Ga_{0.8}As$ quantum wells. The bottom of the wafer was antireflection coated with a 1/2 wave layer of SiN_x to remove any effects of the semi-insulating substrate on transmission properties. This structure is shown in Figure 2-8. Even though the front and back mirrors differ in their number of periods, their reflective properties are similar, for the top mirror also includes the semiconductor/air interface. In-situ measurements and corrections were made at three points during the growth. The first correction was made after half of the bottom mirror was grown. The second was made just after the growth of the cavity region to place the cavity mode at the center of the wafer about 200 Å from the zero bias exciton absorption. The third correction was made just before the complete structure was grown, to ensure that the zero bias response was correct and that no additonal growth was required. The wavelength at which the exciton and cavity mode occurs is 9740 Å, where the GaAs substrate is transparent, allowing light to pass through the device from either side. Additionally, at zero bias, the

9

front and back mirror reflectivities are nearly equal, so that the device characteristics should be the same from the front side and back side of the wafer.
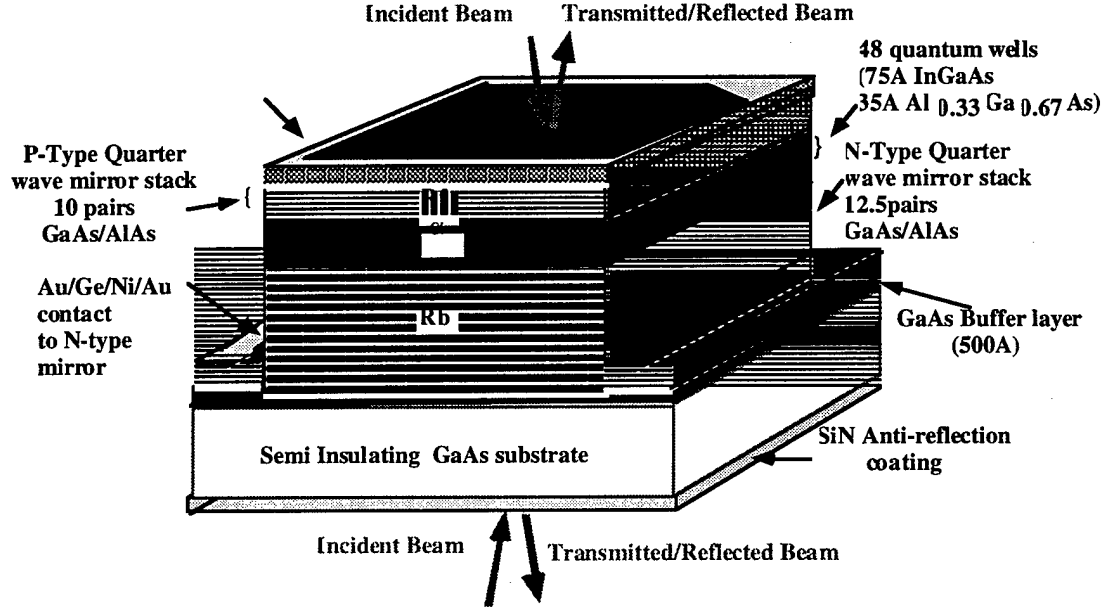

Figure 2-8: Device structure of the X-Modulator

The device can be thought of as a front mirror with electric field reflectivity r_f and an effective back mirror with reflectivity $r_b e^{-\alpha L}$, where α is the quantum well exciton absorption and L is the optical cavity thickness. The device is designed to contain nearly matched front and effective back mirrors at zero applied field. With no bias on the structure, the quantum well absorption peak is at a shorter wavelength than the cavity resonance so that the absorption at resonance is low. From simple cavity theory, the device's intensity reflectivity and transmittivity are given by:

$$R = \left[\frac{r_b e^{-\alpha L} - r_f}{1 - r_f r_b e^{-\alpha L}} \right]^2 \qquad T = \frac{\left(1 - r_f^2\right)\left(1 - r_b^2\right) e^{-\alpha L}}{\left(1 - r_f r_b e^{-\alpha L}\right)^2}$$

As the front and back mirror reflectivities become equal, R becomes zero and T nears unity (for small α). Larger minimum values of α decrease the maximum transmission. Application of an electric field red shifts the lowest energy exciton absorption towards the

10

Fabry-Perot wavelength via the quantum confined Stark effect (QCSE), thus increasing the absorption at that wavelength. Consequently, this increases the device reflectivity R and decreases T. These operating conditions are illustrated in Figure 2-9.
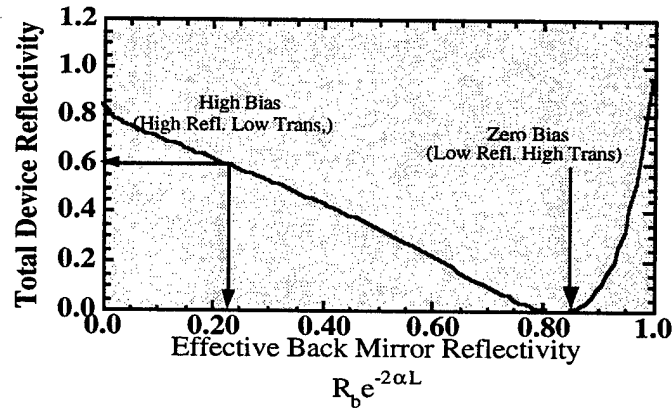

Figure 2-9: Operating conditions for the X-modulator

Using our thin films computer simulations, we can calculate and predict modulation ratio (MR), optical bandwidth (OB), and change in reflectivity (DR) (related to insertion loss) for our devices and study the tradeoffs between them.
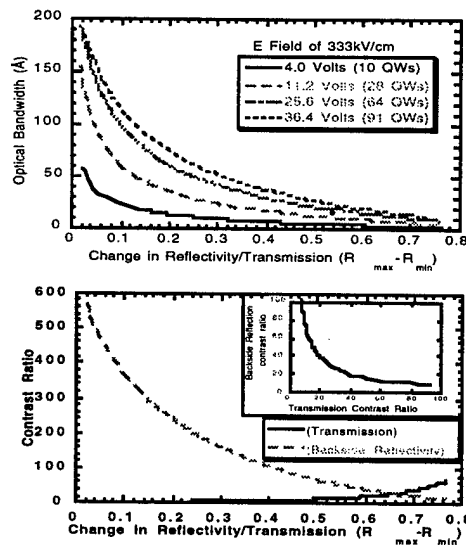

Figure 2-10: Parameter space for X-modulator: Optical bandwidth and contrast ratio vs. change in reflectivity.

11

Figure 2-10 illustrates some of the parameters of interest for an X-modulator. To summarize some of the results found there:

• For fixed voltage, as MR increases, DR increases and OB decreases.
• For fixed DR, as voltage increases, OB increases and MR decreases.
• For fixed MR, as voltage increases, OB increases and DR decreases.

We can control the front and back mirror reflectivities, cavity length, distance in wavelength between the zero bias exciton peak and the Fabry-Perot wavelength, and maximum and minimum absorption to tune a given device for a desired application. Figure 2-11 shows the theoretical and experimental reflectivity and transmission spectra for our device which is shown to switch between 60% and 6% reflectivity and transmission in both states.
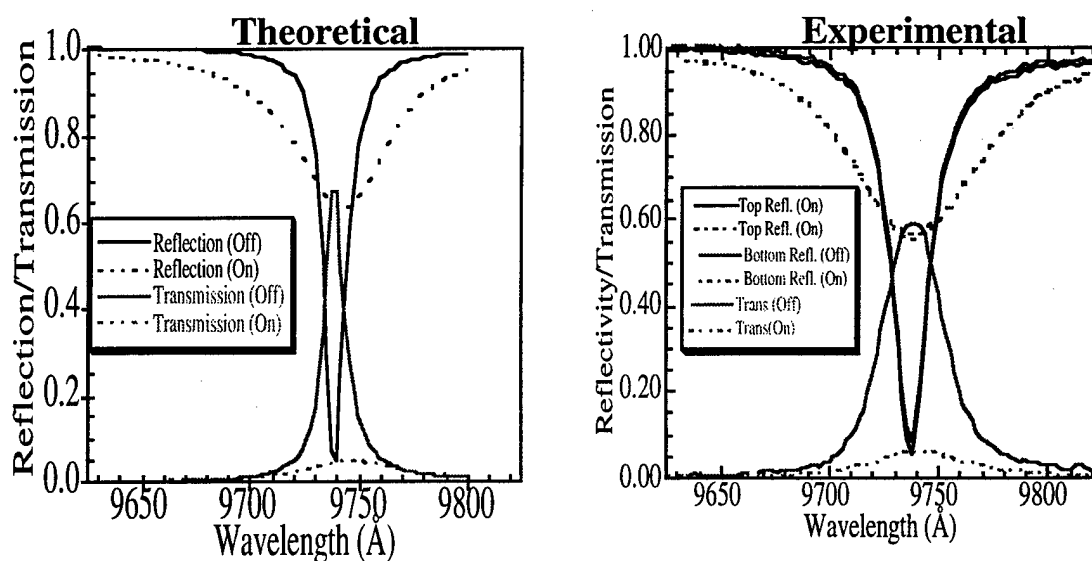

Figure 2-11: Theoretical and experimental curves for reflection and transmission of the X-modulator. "On" indicates response with 40 Volts applied.

Devices which are not symmetric from the front and back sides of the wafer may also be designed, and can result in higher contrast ratios. The contrast ratio of the symmetric device is 10, whereas the contrast ratio of the device simulated in Figure 2-12 is around 80. At the end of this chapter an arrangement of devices is shown which can symmetrize these characteristics, as well as enhance the contrast ratio even further.
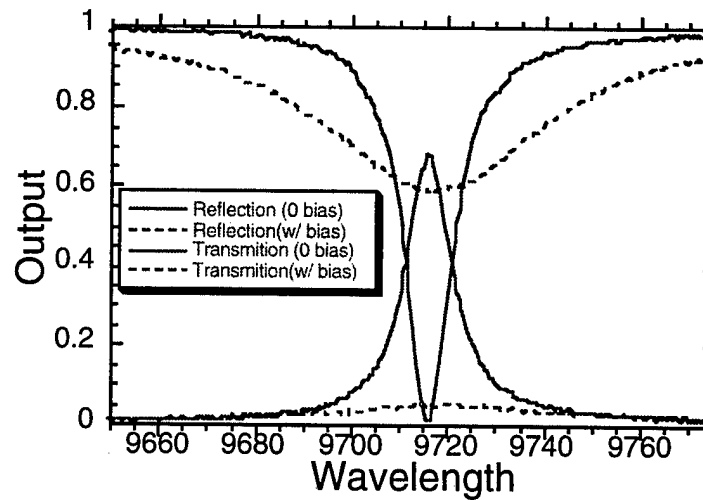
Figure 2-12: Asymmetric X-modulator, better contrast ratio

In order to investigate device stacking, it is necessary to investigate device response at various angles of incidence and for TE versus TM polarized light. Incident angle must be accounted for when designing devices. However, it can be used advantageously to increase device yield in MBE grown wafers which typically display a radial growth nonuniformity. Figure 2-13 shows the zero bias reflectivity spectra for the X-modulator, which was designed for optimal performance at normal incidence (0°). As can be seen from these simulations, for incident angles larger than 25°, the zero bias reflectivity becomes strongly angular dependent. This effect occurs because the Fabry-Perot mode, initially at 9840 Å, shifts as the light sees a different effective optical distance, but the exciton absorption does not shift in the same manner. Thus, the contrast ratio is degraded and we see a split in the TE and TM characteristics. Such dependencies will in turn affect multiple device characteristics such as crosstalk and insertion loss. In addition, we show how the use of a larger cavity can offset angular dependencies. The wider cavity device is designed to be matched to the 9840 Å device with an incident angle of 25°. When designing structures for operation at non-normal incidence, the value of the exciton absorption at a given wavelength could be affected if TE polarized light is not used. This is the result of differences in the amount of absorption of TE and TM polarized light by the heavy hole and light hole

13

excitons. Heavy hole TM absorption is essentially zero while light hole absorption is enhanced for light traveling in the plane of the quantum well material.
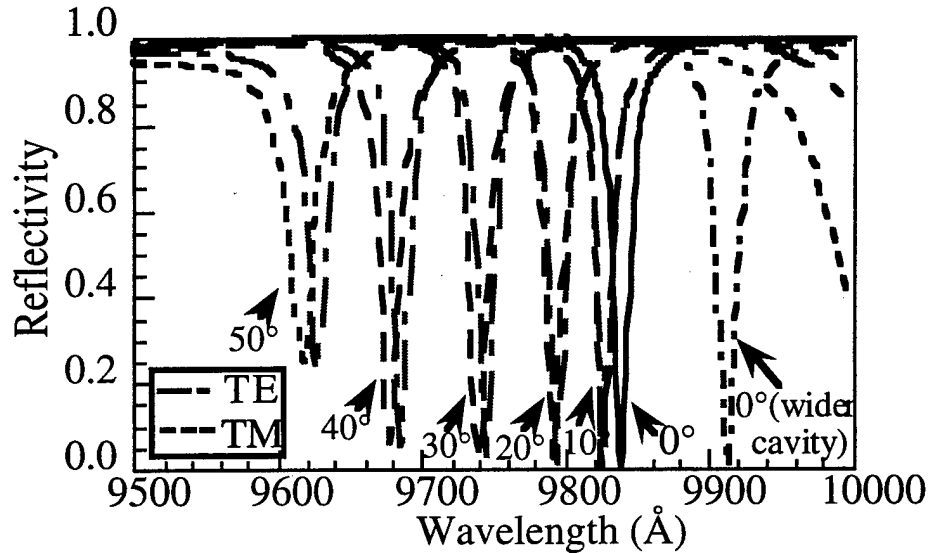

Figure 2-13: Simulation of zero bias reflectivity of X-modulator at various angles using TE and TM polarized light, demonstrating the degradation of the contrast ratio and the TE-TM split. The reflectivity of a wider cavity optimized for 25° is also shown.

2.4 Systems Applications

In this section, we will exhibit some of the possible systems applications of the X- and R-gates. As previously stated, X- and R-gates are useful for computation, coding, switching, and routing. To begin with, we have demonstrated the logic and routing functionality of the X-gate by stacking two of the devices in series and verifying the expected output functions as shown in Figure 2-14. Because large optical output is available in both states, an incident optical signal at A or B could be routed to any of the three optical outputs, depending on the state of the electrical inputs, D and E. We theoretically predicted and experimentally verified the logic performance of two stacked 200 μm x 200 μm square X-modulators. Light incident at 21° off normal incidence was used, which imparted a 50Å blue shift to the Fabry-Perot resonant wavelength. For these measurements, only input A was an 'on' optical signal, making the outputs D, D'E, and DE' for outputs 1, 2, and 3

14

respectively. Output 1 represents the single device reflectivity response as shown previously in this chapter. The figure here shows the logic high and some of the various logic low levels at the FP wavelength for outputs 2 and 3, given the various combinations of the electrical inputs.
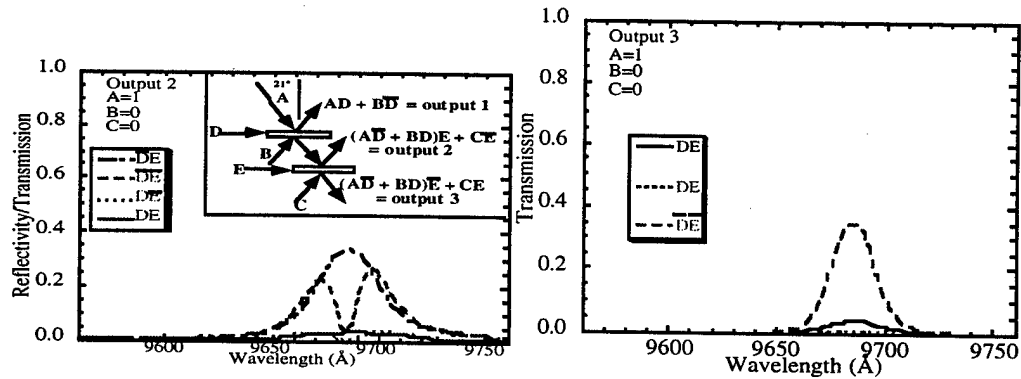

Figure 2-14: Measured signal versus wavelength for output 2 and output 3 (shown schematically in inset) of a dual stacked X-modulator system. Output 1 is similar to the plots shown in Figure 1 with the appropriate wavelength shift.

A single X-gate with an electrical control signal performs a simple 2x2 exchange operation. This operation is useful for sorting and routing networks. Using regular arrays of these devices as shown in Figure 2-15 we can easily construct an 4x4 (or in general, an NxN) optical crossbar switch, permuting the 4 optical inputs to the 4 optical outputs in a conservative manner (number of 1's is preserved). Crossbar design issues include reconfiguration time, signal bandwidth, total data throughput, and data word size. Optical crossbars such as the one shown here should outperform electronic versions in all of these areas. The reconfiguration time for the network shown should be around 0.1 nsec, the signal bandwidth is large because the data path is all optical, and the data throughput can be large because many lines can be switched in parallel, as can the data word size.
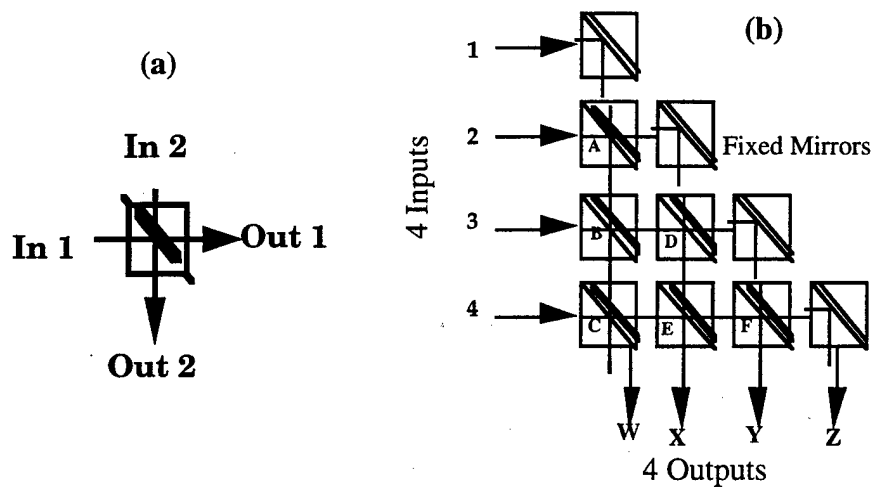
Figure 2-15: (a) Schematic representation of X-gate, (b) 4x4 optical crossbar using 6 X-gates in a regular triangular array.

For simplicity we will first examine the 4x4 crossbar switch shown in Figure 2-16. The minimal implementation of the 4x4 crossbar requires only 5 X-gates and is shown in Figure 2-16 along with a schematic representation of how this switch might be realized using stacked devices. This implementation of the crossbar may also be flattened onto a single wafer layer with a few mirrors placed around the structure (a multi-bounce type architecture) as shown in Figure 2-17.
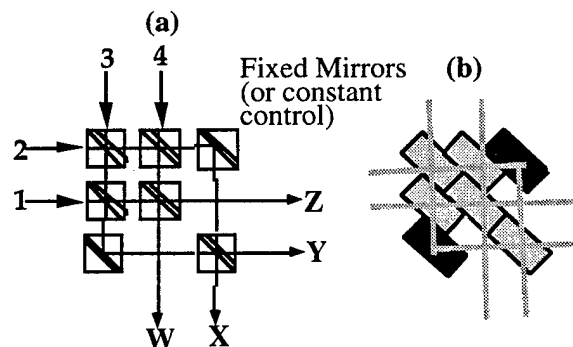

Figure 2-16: Minimal realization of 4x4 crossbar with 5 X-gates

Figure 2-18 depicts the worst signal to noise ratio for any of the output channels over all of the possible voltage switching configurations given optimally symmetric individual X-modulators with the given changes in reflectivity/transmission ($R_{on} - R_{off} =$

16

$T_{on} - T_{off}$) and contrast ratio ($T_{on}/T_{off} = R_{on}/R_{off}$) for both the 5 and 6 element realizations. It is also possible to use asymmetric device structures (where $T_{max} \neq R_{max}$) and vary other device parameters to adapt optimal X-modulator device structures to specific systems applications. A 3-D interconnect arrangement using stacked wafers of X-modulator arrays is envisioned to replace previous interconnect technologies because of its fast reconfiguration time, high signal bandwidth, and potentially high data throughput. As a routing device, the X-modulator whether electrically or optically controlled is very promising. Regular arrays of X- or R-gates (i.e. 2-D and 3-D stacked structures of quantum well devices) can also be used to realize field programmable gate arrays (FPGAs) and other more complex functions (such as a full adders and other logic units). Figure 2-19 shows an optical FPGA implemented using X-gates in a binary lookup table fashion, which is essentially the triangular crossbar switch above with the devices rotated by 90°. The conservative and reversible nature of the X- and R-gates can be efficiently utilized in automatic logic synthesis and layout (CAD). The all optical full adder of Figure 2-20 was obtained using a synthesis approach, and is realized with only 5 X-gates (and one for fan-out).
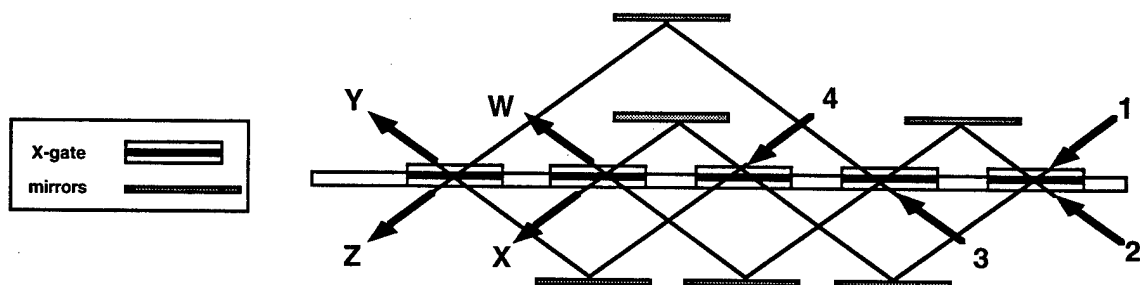

Figure 2-17: Single Wafer plane realization of 5X-gate 4x4 crossbar switch

This implementation would require optically controlled devices or some optoelectronic conversion between devices.
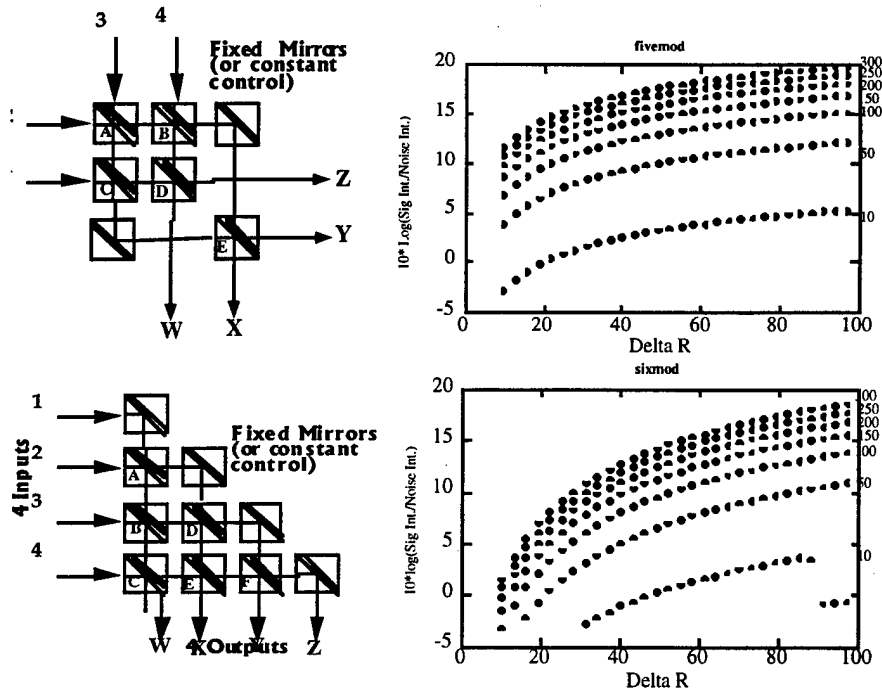
Figure 2-18: Worst case signal to noise ratios for 5 and 6 X-gate 4x4 crossbar switches versus change in reflectivity (ΔR) with contrast ratio as a parameter
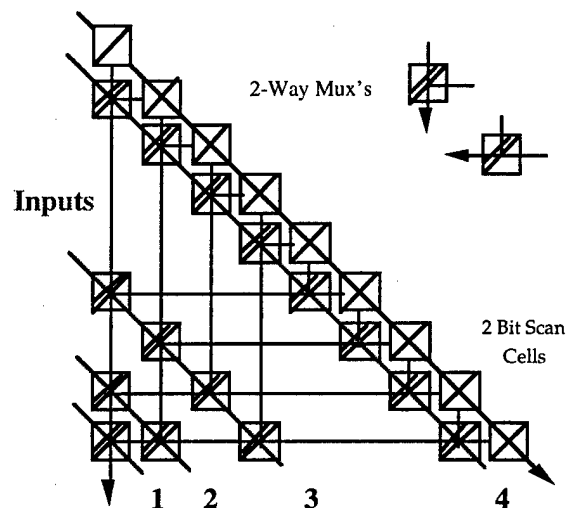

Figure 2-19: Optical implementation of an FPGA using X-gates in a binary lookup table
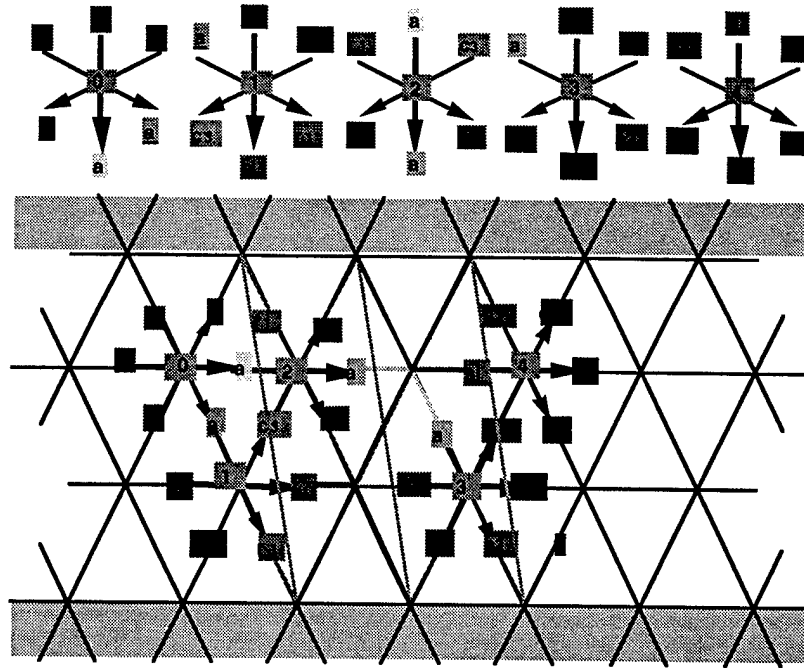
Figure 2-20: All optical full adder implemented with 5 X-gates

Larger crossbar switches can be assembled from smaller 2x2 or in general N by N crossbars in various configurations. For example, we could simply extend our triangular array of devices to an NxN array. However, the number of devices required by this arrangement grows as N^2, which is usually an unacceptable complexity. Numerous other networks have been proposed in the literature, for example that of Figure 2-21, which indicates how larger crossbars may be built up recursively from smaller ones. The figure also compares the number of devices needed for a regular triangle implementation to a smarter method. All of these networks may be realized with our X- and R-gates. In most cases, even the implementation shown in the figure is not the minimal realization. For example, Figure 2-22 demonstrates how an 8x8 crossbar can be constructed with only 12 2x2 switches. Some of these proposed networks are more adapted to our technology than others.

19

Extended Crossbar System

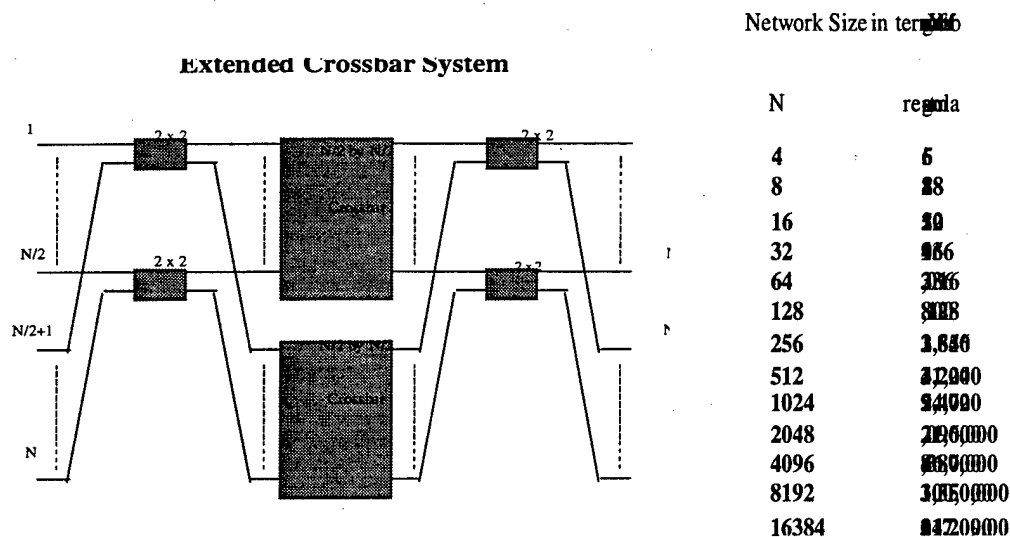| N	regular
4	6
8	28
16	49
32	166
64	386
128	898
256	2,846
512	12,000
1024	44,000
2048	196,000
4096	880,000
8192	3,850,000
16384	14,200,000

Figure 2-21: Construction of a larger crossbar switch using smaller crossbars. Comparison of the number of X-gates required for this implementation compared to a regular triangle array.
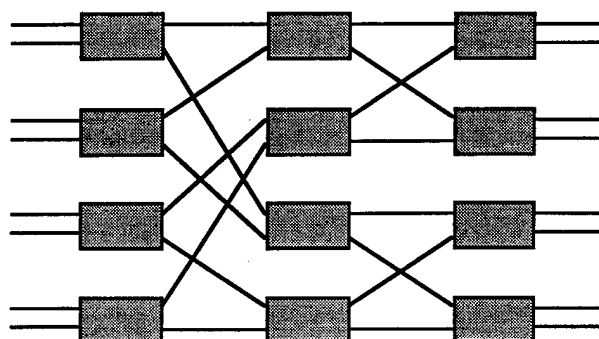

Figure 2-22: 8x8 Crossbar switch

2.5 Refinements for Optical Switching Systems

It is clear that our proof of concept devices are not ideally suited to systems applications. In this section, we begin to address three specific aspects of the structures which should make them more amenable to use in a systems context. First of all the voltages at which the initial device operated (40 Volts) is much too large to use in an optoelectronic system or to integrate with electronic systems. A partial solution for this problem is experimentally proven feasible. Second, although we term our devices 'power-conserving', the maximum transmission is still only 60-70%, which will lead to problems with fan-out and cascading of devices. One method of increasing this maximum

transmission or reflection is described, which involves incorporating forward biassed quantum wells into the Fabry-Perot cavity to provide gain in addition to the lossy quantum wells to modulate the absorption.

2.5.1 Voltage Reduction

The high voltage of operation in the original X-modulator is partially due to the use of strained 75Å $In_{0.2}Ga_{0.8}As$ quantum wells. The use of this strained material requires the use of large, 200 Å AlGaAs barrier regions to reduce the overall active region's Indium concentration and hence strain. This reduced strain permits the structure to be below the Matthew's-Blakesly critical thickness. Beyond this limit the crystal relaxes and the exciton resonances are quenched. As a first step towards reducing these voltages we have used a graded buffer region and strain compensation techniques to reduce the thickness of the barrier regions to 100Å and the required switching voltage of a similar structure by ~35%. In this technique, the bottom and top mirror layers are varied in composition from 0% Indium at the substrate up to about 12% indium at the onset of the quantum well region. This 12% value is chosen so that the alternating barrier and well layers, which are strained in opposite directions (tensilely and compressively), compensate each other and thus result in approximately zero net strain. This graded structure is illustrated in Figure 2-23. The photocurrent data for this structure both with 200Å barriers and 100Å barriers is shown in Figure 2-24. The thickness of the active region was reduced by 40% and can probably be used to reduce it by about 60% with even thinner barriers. This reduction in active area thickness increases the effectiveness of the applied field. As can be seen in the figure, at 5 Volts the exciton shifts by 30 Å in the thick barrier case and 100Å in the thin case, and at 10 Volts, 130Å compared to 320Å.
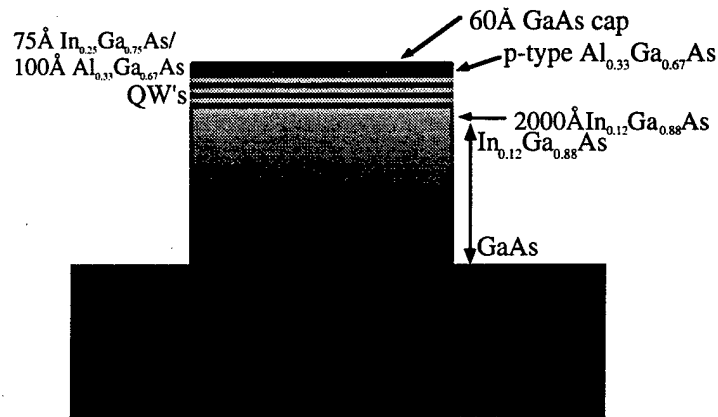
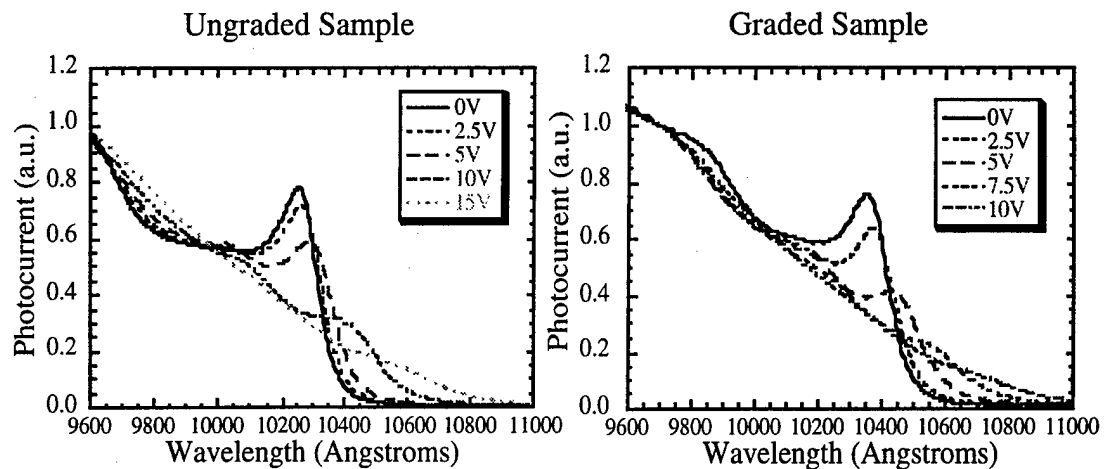*Figure 2-23: Device structure of graded buffer device.*

Figure 2-24: Photocurrent data for graded buffer region, showing voltage enhancement.

5.5.3 Dual Zone Structures

As previously mentioned, our test devices as originally designed have a maximum transmission of 60-70% and a minimum transmission of about 6%, hence a contrast ratio of 10. Ideally these percentages should more closely approach 100% and 0%, or possibly even greater than 100% in the maximum transmission case (i.e. amplification) for fan-out purposes. We are attempting to overcome this problem by investigating structures that include two layers, or zones; one that performs the modulation of the light (X-modulator, for example) and one that will amplify the light, in essence restoring the energy that is lost in the modulator.

As an initial design for such a device, we consider two possible configurations. In the first configuration, the gain quantum wells are contained within the same Fabry-Perot cavity as the absorptive wells, as shown in Figure 2-25. In this structure there are two individually biased regions, so that we end up with a n-i-p-i-n stacking of layers. The gain layers are forward biased to provide a gain of approximately 600 cm^{-1} per well, and the absorptive wells are switched between around 11,000 and 50 cm^{-1} per well loss using the quantum confined Stark effect. It may also be desirable to switch the gain layers between gain and loss, however the speed of this switching is limited by the amount of time required to sweep the carriers out of the quantum well region. We have simulated the device in the case that only the absorptive wells are switched. The results of this simulation are shown in Figure 2-26. As can be seen in the figure in one state, the device is highly reflective (95% reflection, ~0.3% transmission). Other structures may produce a higher reflectivity than 95%, but are more difficult to correctly grow using MBE. In the transmissive state, the device amplifies the signal transmitted by a factor of ~2 (with ~5% reflection). Thus, we have demonstrated that our devices can incorporate gain layers within the optical cavity to restore some of the light lost to absorption. The optimal reflection and transmission percentages depends upon the architectural configuration of the devices involved. In some cases an asymmetric device such as this may be an acceptable solution or even desirable (for example for use in tapped delay lines). By simply changing the reflectivity of the front mirror, this device may be transformed into a reflection modulator with gain. The simulated results for this device are shown in Figure 2-27, where the device switches between 110% reflection and reflectivity near zero.

A second possible device structure would consist of two cavities, where the coupling between the modulator cavity and the gain cavity is small to prevent coupled cavity effects. In this case, a large reflectivity mirror is required between the two cavities, which results in a high Q modulator and makes our design difficult to realize. A better solution may involve anti-reflection coating the top of the device so that there is essentially only one cavity present. In this case, the gain layers are only single or double pass depending on the state

23

of the device and thus a larger number of wells would be required. We feel that the first configuration is the more promising of the two, however both designs are under investigation. The growth and fabrication of these devices would be more complicated than that of a single X-modulator, but similar work has been done at Stanford integrating modulators and LEDs.
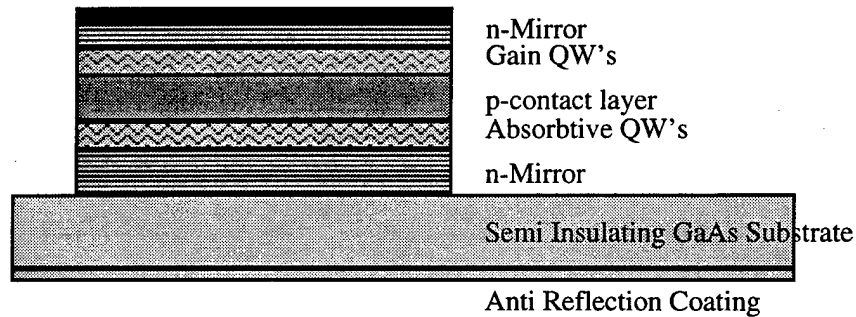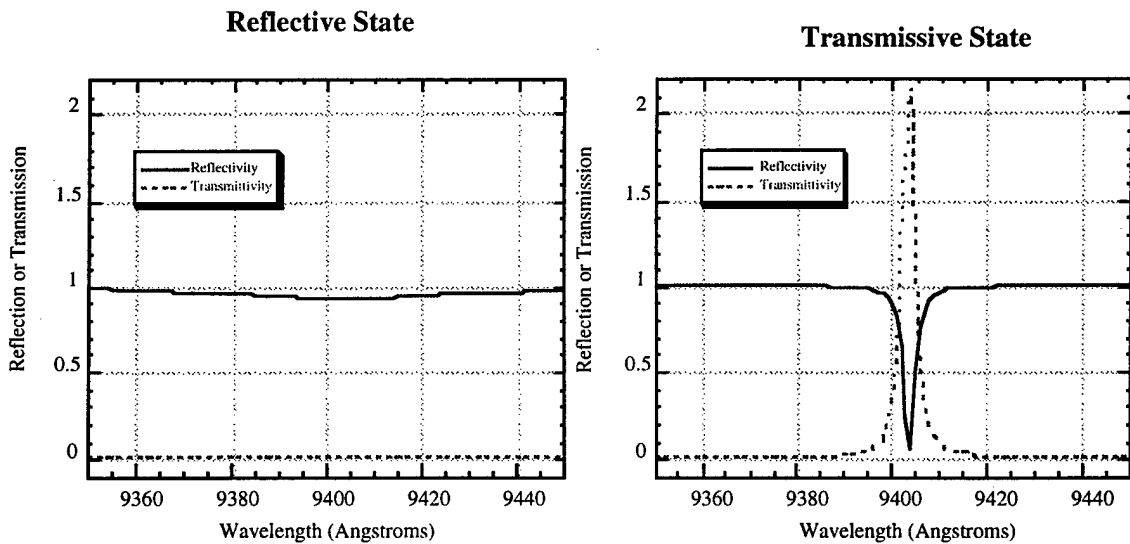

Figure 2-25: X-modulator with gain layer

Figure 2-26: Simulation of dual zone reflection/transmission modulator with gain.
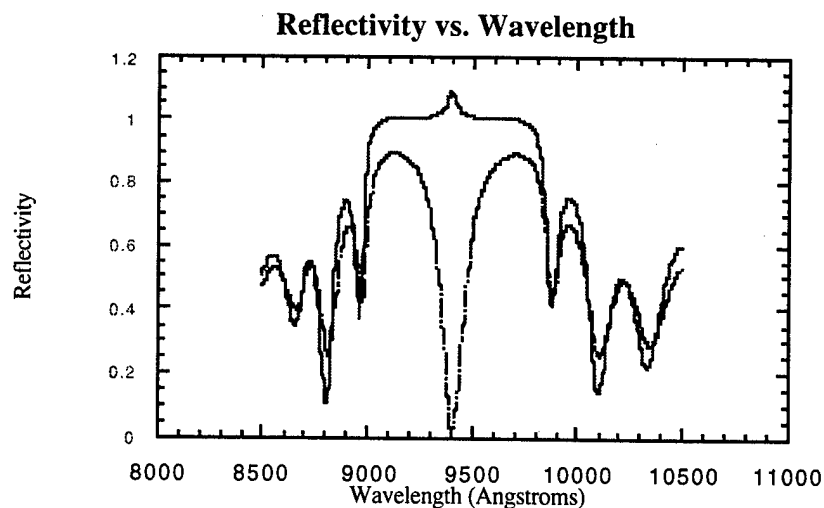Contrast ratio asymmetry between the two states

24

Reflectivity vs. Wavelength

Figure 2-27: Dual zone reflectivity modulator with gain, contrast ratio > 1000

2.6 Conclusions

We described the design, fabrication, and testing of vertical cavity X-modulators--structures which allow for conservative invertible switching.   Unlike earlier modulator structures which modulate either the amplitude or the phase of light, these modulators act to modulate the direction of the input light without changing the output intensity or phase. We have discussed the use of X- and R-gate devices for routing and other computation, as well as some aspects of these devices that make them amenable to photonic switching and routing. Finally, we have described refinements to the original X-gate design (both current and future) that will make them much more useful for systems applications. X-modulators should have a significant impact on efficient switching, as well as 2-D and 3-D array optical switching, routing, and logic.

Chapter 3: High Speed Properties of Vertical MQW Modulators
3.0 Introduction

The circuit-switched public network infrastructure is continuously stretched to its limits in order to provide support for bandwidth hungry applications running at speeds

set by Moore's law due to the limitation of electrical interconnections: high power consumption, and poor signal integrity due to crosstalk, signal skew and termination limitation. Free-space smart-pixel optical interconnect architecture promises to relieve the interconnect bottleneck in high-speed parallel interconnection and switching systems. It offers the following attractions: high bandwidth with data rates of > 20Gbit/s and higher, and extendable further through WDM techniques; low power requirement, skew and crosstalk, high reliability due to lack of physical contact (line capacitance or mutual coupling) and potential for high density i/o.

Vertical cavity resonant enhanced multiple quantum well modulator, which consists of semiconductor quantum wells grown in a Fabry-Perot cavity configured as a p-i-n diode (see Fig 3-1). Applying electric field across the diode increases the cavity absorption via quantum Stark effect (QCSE), therefore the reflectivity of the incident beam (see Fig 3-2). Because the resonant cavity enhanced effect at the working wavelength, it requires fewer quantum wells to absorb the same fraction of the incident light, and therefore can operate at a lower voltage with high contrast ratio. Compared to waveguide structure, its vertical cavity structure takes less real estate area on the chip and makes it easy to be integrated with Si devices through flip-chip bonding and implement dense 2 dimensional arrays.
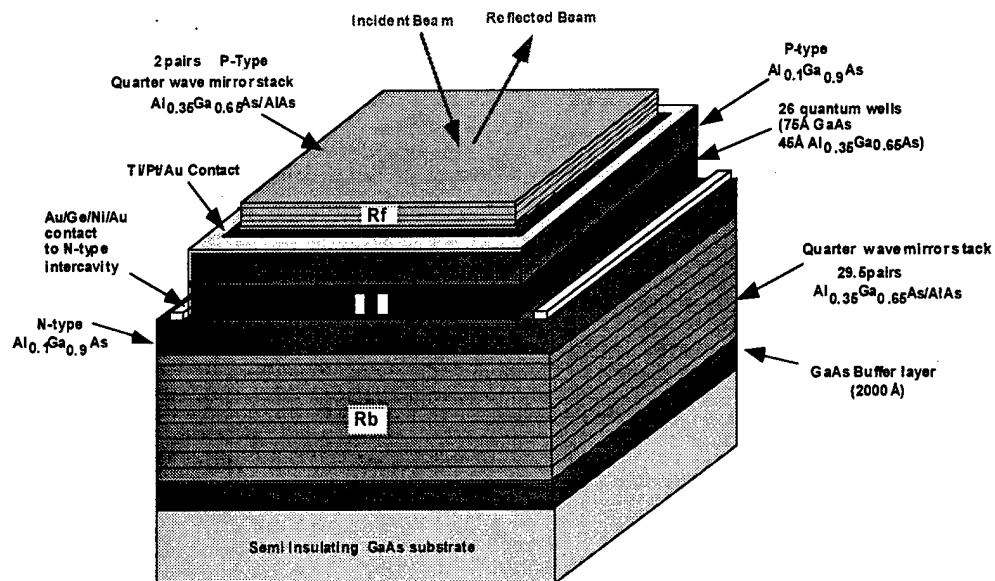

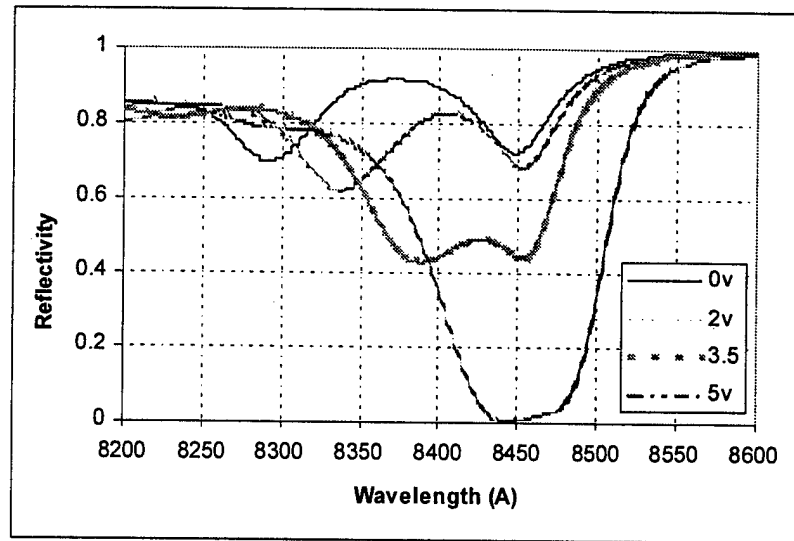*Fig 3-1: High speed vertical cavity MQW modulator*

Fig 3-2   Reflectivity of vertical cavity MQW modulator

High speed modulation is one of the keys for future optical switching and interconnecting networks. Electrical control of optical modulation employing quantum well (QW) excitons based upon electro-optical effects, such as the quantum confined Stark effect QCSE), will be limited in speed by the RC time constant of the device itself at low optical intensity. However, at high optical intensity, the large number of photogenerated carriers in the intrinsic region will limit the high speed performance of the device through space charge screening, photo-current related voltage drop and exciton saturation. We focused on the optimization of high speed, low driving voltage and high optical power of the devices.

3.1   Design of high speed modulator

For most of the applications, we want the device to have low driving voltage, high contrast ratio, low chirp and high saturation power, and most of all high speed. However there are some trade-offs , and we will examine them below.
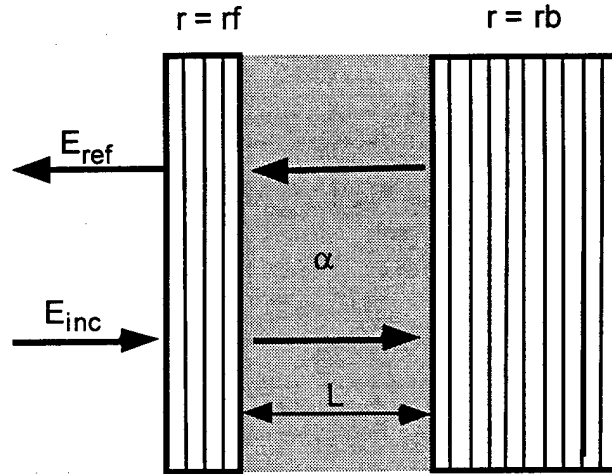
Fig 3-3 Vertical cavity MQW modulator schematic

The electroabsorption effect is the fundamental effect for the operation of the vertical cavity MQW Fabry-Perot cavity. The device can be thought of a front mirror with electric field reflectivity rf, a back mirror with effective field reflectivity rb and a optical cavity with absorption α, cavity length L as shown in Figure 3-3. The reflectivity of normal incident optical beam at resonant wavelength, where the cavity length L is an integral number of half-wavelength is:

$$R = \left[\frac{rb \cdot e^{-\alpha L} - rf}{1 - rf \cdot rb \cdot e^{-\alpha L}} \right]^2$$

The device is designed to have minimum absorption α_{min} with zero bias and maximum absorption α_{max} with vertical electrical bias via quantum confined Stark effect (QCSE) . Between these two biases, the reflectivity changes from maximum R_{on} to minimum R_{off} given by:

$$R_{on} = \left[\frac{rb \cdot e^{-\alpha_{min} L} - rf}{1 - rf \cdot rb \cdot e^{-\alpha_{min} L}} \right]$$

To have large contrast ratio, we have matched the effective back mirror reflectivity to

$$R_{off} = \left[\frac{rb \cdot e^{-\alpha_{max} L} - rf}{1 - rf \cdot rb \cdot e^{-\alpha_{max} L}} \right]$$

the front mirror, such that:

$$R_b \, e^{-2\alpha_{max} L} = R_f$$

28

Simulation has shown that the quantum width of 75Å since the maximum absorption change $\Delta\alpha_{max}L_z$ peaks near $L_z = 75$Å with a value of 0.012 for GaAs/Al$_{0.33}$Ga$_{0.67}$As quantum wells, and give us the largest contrast ratio.

The switching voltage is ultimately determined by the quantum stark shift, spacing between excitonic wavelength and Fabry-perot dip, and intrinsic region length d . The exciton peak red shifts is proportional to the 4th power of well width and quadratic to the electric field across the well region. Use wider well will decrease the switching electric field, while decrease the exciton absorption strength and we will need to use more quantum wells to balance the cavity at minimum reflection. This will not only increase the intrinsic region width, but increase the switching voltage as well. We place our exciton peak 15Å away from Fabry-perot dip, which will give us a switching voltage of 5V. Decrease the spacing between these two can decrease the switching voltage, but it will decrease the contrast ratio as α_{min} increases.
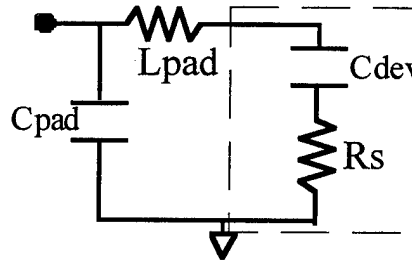

Fig 3-4 Equivalent circuit of high speed device

The equivalent circuit of the device at low optical intensity, which is typically that of a simple reverse biased p-i-n diode, is shown in *Fig 3-4*. Charging and discharging of the device capacitance, limits the ultimate practical switching time to be

$$f_{3dB} = \frac{1}{2\pi\left[C_{dev}(R_s+Z_0)+C_{pad}Z_0\right]}$$

The capacitance of the device itself can be modeled as a parallel plate capacitor with fringe capacitance. It decreases as as the device gets smaller, but fringe capacitance will ultimately plays a significant role. Our smallest device is 20umx20um. Further decrease the size won't decrease the capacitance and will only increase the resistance of the device as observed by the experiment. Increase the intrinsic region with d will decrease the capacitance of the device, but it will increase the switching voltage as well. We use intercavity n contact since the back DBR mirrors have large serial resistance due to the carrier transport during the heterojunctions..

At high optical intensity, both space charge screening and exciton saturation will depend on the carrier concentration in the intrinsic region. To minimize the carrier sweep-

out time, we decrease barrier height and width (45Å $Al_{0.35}Ga_{0.65}As$) to minimum yet maintain enough quantum confinement and absorption ratio. The electrical field of intrinsic region with different intercavity layer thickness carrier distribution of under 5kw/cm² optical illumination intensity and 3V reverse bias is shown in *Fig 3-5*.
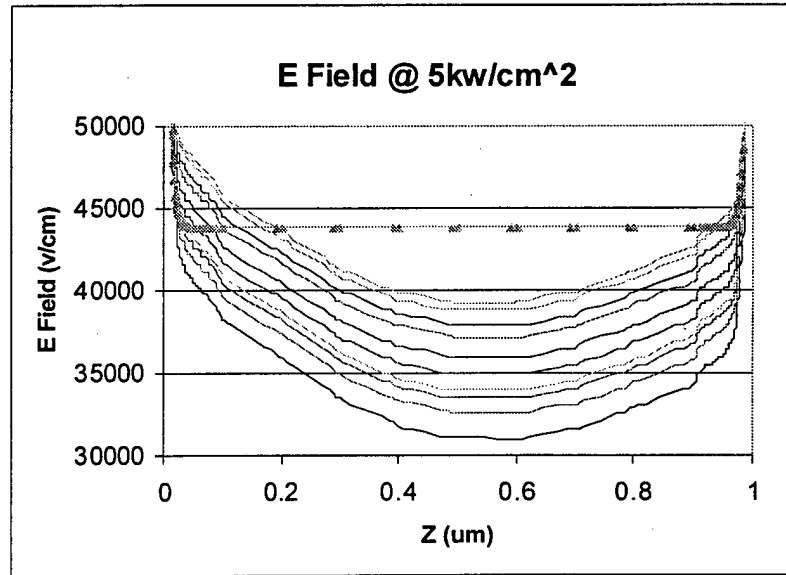

E Field @ 5kw/cm^2

Fig 3-5 Electrical field of intrinsic region under 5kw/cm² illumination (As comparison dotted line is the electrical field with no illumination)

The electrical field is not uniform due to the photogenerated carriers in intrinsic region. The first order of the absorption to the first order is linear with the electric field, therefore the ultimate reflectivity of the device, which is determined by the total absorption inside the cavity, is only dependent on effective voltage across the intrinsic region. The effective voltage across the intrinsic region under different optical illumination as a function of intercavity layer thickness is shown in *Fig 3-6*. It decreases as we increase the optical power and decrease the intercavity layer thickness, especially when the layer thickness is smaller than 1μm. The additional voltage drops along the later resistance due the photocurrent generation. We choose the n doping thickness of 1μm so that our device can handle high optical power, which ultilmately determines the fan-out and signal-noise-ratio of the system. Further increase the n doping thickness will affect the high speed performance of the device due to the increase of fringe capacitance and resistance of the device.
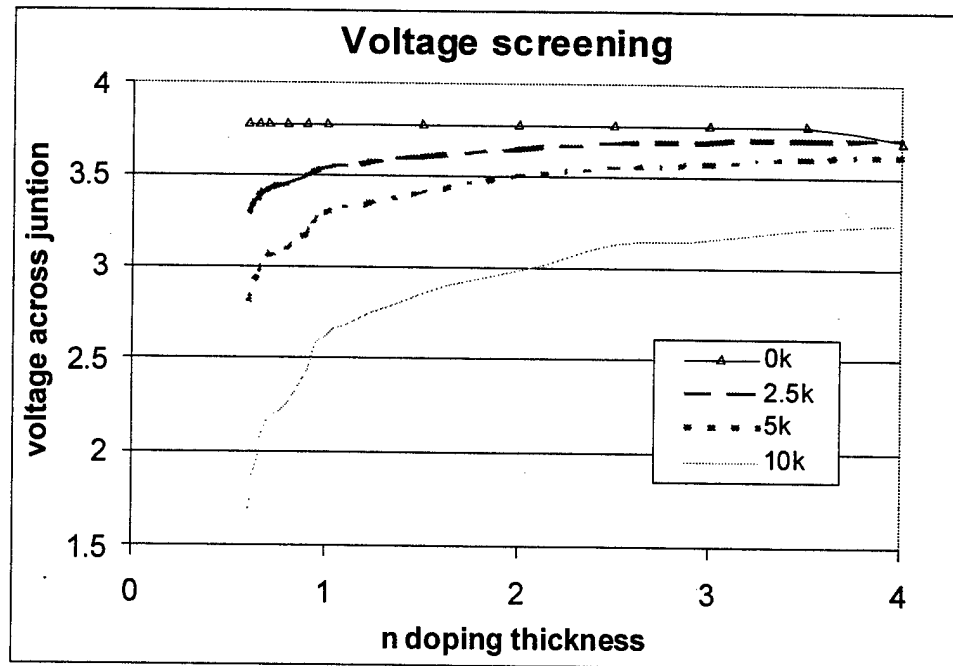
Fig 3-6 Effective voltage drop across the intrinsic region under different optical illumination as a function of n doping layer thickness
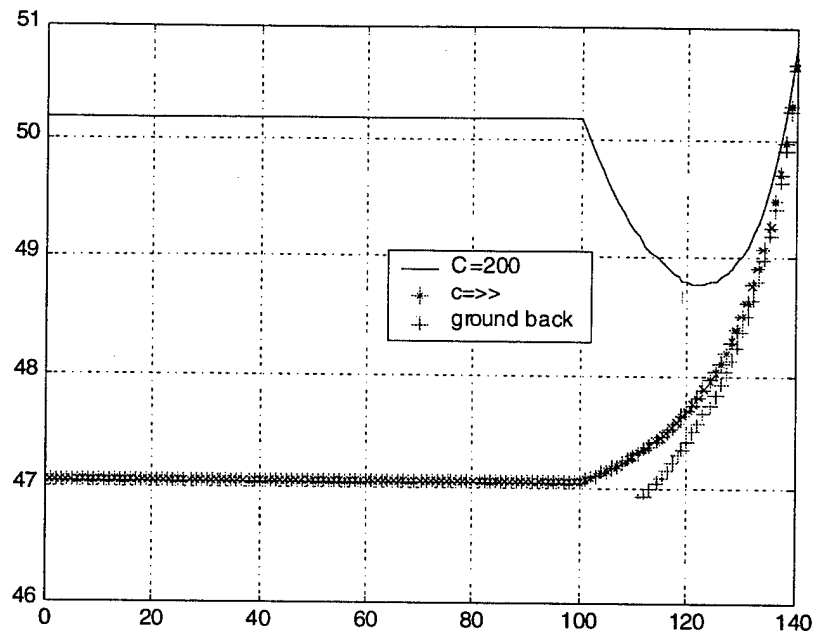

Fig 3-7 Characteristic impedance of microwave probe pads size of 100um &150um spacing and 40um long tapered feedline.

Coplanar microwave probes are integrated with high speed device for wafer level probing and testing. To minimize the parasitic capacitance of probe pads, the n doping region underneath probe pads has been etched away and filled with low dielectric material (ε_r = 2.5 up to 20GHz) Cyclotene Advanced Electronics Resins (Photo-BCB). The spacing between the probes and feed line are designed so that the characteristic impedance of them are about 50Ω that of the impedance of microwave source as shown in *Fig 3-7*. In comparison, the similar structure with infinite ground signal line width and back side ground plane are plotted as dotted lines.

3.2 Device processing

The epitaxial structure we discussed for high speed operation is shown *Fig 3-1* and was grown on a semi insulating GaAs substrate at 450°C by molecular beam epitaxy (MBE). We fabricate the devices using the process steps outlined in *Fig 3-8*, and they include 1) P contact etch, metal evaporation and lift-off 2) N contact etch 3) N metal evaporation and lift off 4) mesa etch 5) Photo BCB processing 6) Transmission line evaporation and lift-off.
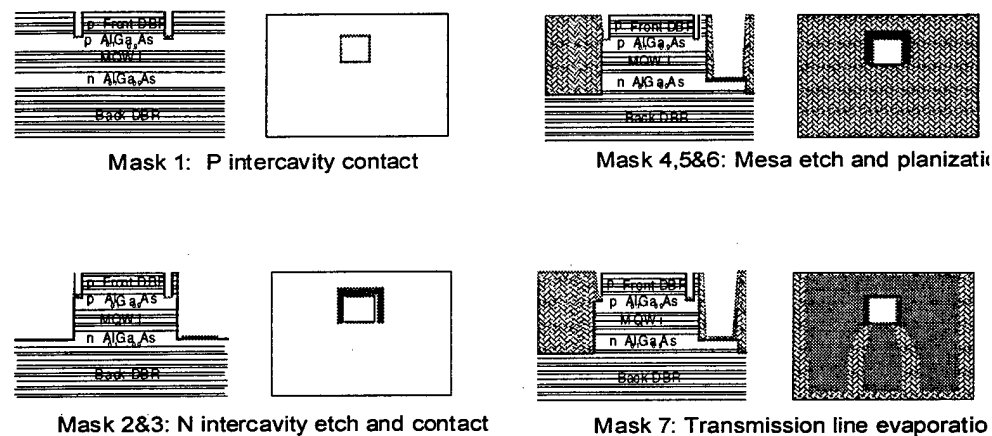
Mask 1: P intercavity contact

Mask 4,5&6: Mesa etch and planization

Mask 2&3: N intercavity etch and contact

Mask 7: Transmission line evaporatio

Fig 3-8 Processing steps for high speed modulator
with integrated microwave probe

For the first step, we evaporate and lift-off Ti/Pt/Au (250Å/400Å/1000Å) P contact after first etch through the front mirror stacks using wet etching (H_2SO_4:H_2O_2:H_2O / 1:8:160). Titanium makes contact adhere to the wafer while platinum in the P contact helps preventing gold diffusion in subsequent processing.

Using second mask, we Cl_2 reactive-ion-etch (RIE) through intrinsic to n doped intercavity region, followed wet-etch to smooth the surface and damage caused by RIE.

And we evaporate and lift-off Au/Ge/Ni/Au (400Å/120Å/125Å/1000Å) n contact using n contact mask.

After further RIE etch through n doped region to form the mesa, we use Photo BCB (Cyclotene 4024) to planarnize the device so that coplanar transmission line and microwave probe can be evaporated and lift-off later using the last mask. The processing steps of Photo BCB are very similar to that of regular photo resist, which include soft bake, expose, develop, cure and descum.

3.3   Measurement Setup and results

The devices are tested under high-speed measurement system (see *Fig 3-9*), which consists of Cascade Probe Station, tunable diode laser source coupled by multi mode fiber to the microscope, New Focus high speed photo detector and HP 8510C Network Analyzer.   And some microwave characterizations of the electrically controlled modulators were obtained on the device as small as $10\mu m \times 10\mu m$.
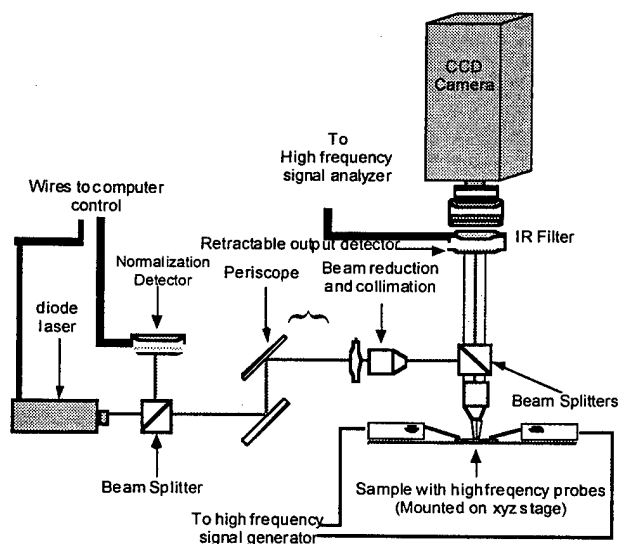

Fig 3-9. High speed set-up for microwave characterization

The equivalent circuit of the devices can be extracted from network-analyzer measurements of devices and calibration probe pads (short, open).   And the measured circuit models for different devices are shown as *Fig 3-10*:
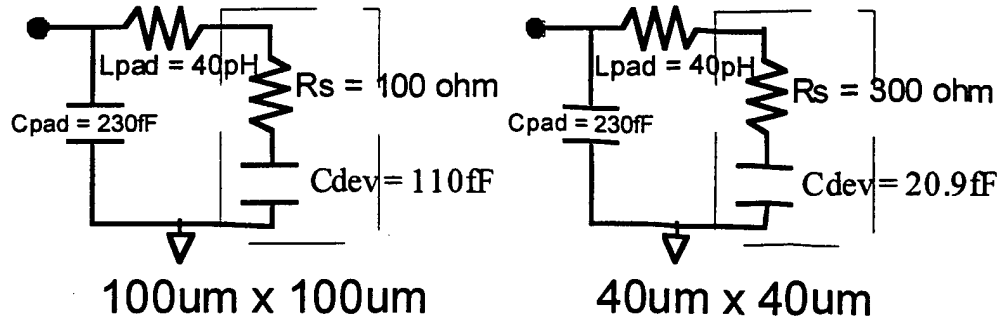
Fig 3-10 Measured equivalent circuit of devices

Also, device impedances of different sizes and under different reverse bias voltages are measured (*Fig 3-11*). The impedance decreases as we increase the bias voltage due to the decrease of device capacitance Cdev, especially around 0V because of the junction is not fully depleted. And the effect is somewhat smaller between 2V and 4V because the junction is already fully depleted after 2V. The impedances decrease as the decrease the device size due to the decrease of device capacitance, however difference is very small between 7um and 12um devices due to the fringe capacitance of the devices.
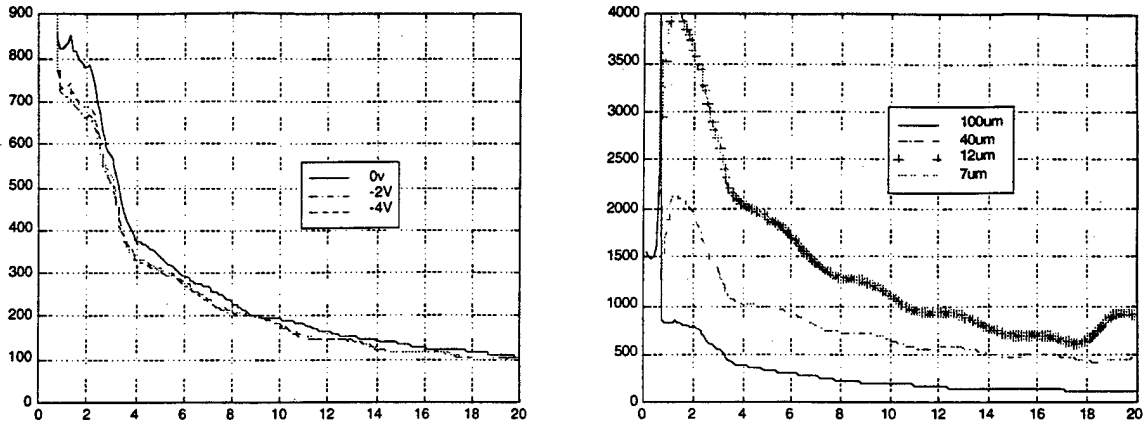

Fig 3-11 Measured device impedances of
Different sizes and with different bias voltage

The RC-limited bandwidth predicted by the measured circuit model is

$$f_{3dB} = \frac{1}{2\pi \left[C_{dev}(R_s + Z_0) + C_{pad}Z_0 \right]}$$

and is 9.6GHz for 100μmx100μm device and 11.8GHz for 40μmx40μm device.

The high speed performance of modulator is RC limited for small switching optical power and after de-embedding and pad parasitic removal, the actural modulation frequency is 12GHz (*Fig 3-12*). The device is switching –5V and –1V, and the measured optical signal is about 3mv.
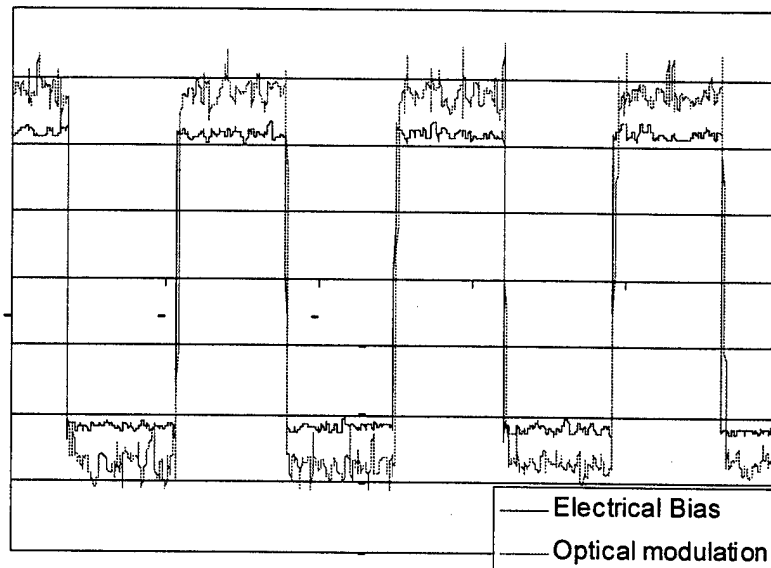
Fig 3-12 Measured digital modulation of device under 3mw optical illumination

Higher frequency could be achieved on smaller devices if we increase the signal to noise ratio of the system.

Chapter 4 — Semiconductor in-line fiber optic devices

4.0. Introduction

One of the major breakthroughs in fiber optic communications was the Er-doped fiber amplifier, which not only provided a broadband optical amplifier, but a new paradigm of active in-line fiber devices. This has resulted in significant research effort directed toward the development of in-line fiber devices, where the evanescent wave coupling is achieved by bringing a side-polished single mode fiber into close contact with a high-index waveguide. This device concept leads to low insertion loss fiber devices and robust, inexpensive packaging. In addition, due to the very strong wavelength selective nature of evanescent wave coupling between two dissimilar waveguides, these in-line devices readily lend themselves to wavelength division multiplexing (WDM) applications.

In-line fiber devices with electro-active materials have been implemented using liquid crystals, electro-optic polymers and lithium niobate substrates. Gallium arsenide and other compound semiconductor devices offer significant advantages over the above materials in that they can be monolithically integrated with lasers and high-speed control electronics, thereby reducing fabrication costs. However, the high refractive index of GaAs provides challenges to coupling to low index fibers.

4.1 A filter

We have demonstrated the implementation of a GaAs/AlGaAs in-line fiber filter. The filter, employing a ARROW (anti-resonant reflective optical waveguide) configuration, consists of a AlGaAs core layer, and an AlAs/AlGaAs distributed Bragg mirror (DBR). When the wafer is attached epi-side down to a side-polished single mode fiber, waveguiding is achieved in the core layer by reflection from the DBR and total internal reflection from the fiber cladding. The schematic of the device structure is shown in Figure 4-1.
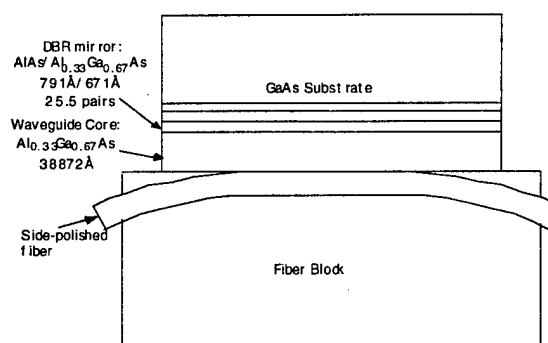

Figure 4-1: Schematic diagram of the in-line fiber filter.

The difficulty in phasematching the modes of the semiconductor waveguide and the glass fiber, which are made of two materials with vastly different refractive indices, is overcome by the use of the Bragg mirror, which is designed to provide high reflection for a specific mode angle. The optical wave in the semiconductor waveguide can therefore propagate with very low effective indices, making it possible to phase match to the single

36

mode fiber. Light couples from the fiber to the ARROW when the effective index of the highest order confined ARROW mode is matched to that of the fiber. Because the two waveguides have very different dispersion curves, phasematching occurs only at specific wavelengths.

The epi-layers of the ARROW were grown by molecular beam epitaxy (MBE) on a GaAs substrate. The AlAs/$Al_{0.33}Ga_{0.67}$As DBR was designed to provide maximum reflectance (R≈1) at an incident angle of 25 degrees, which is the mode angle needed for phase matching. The bandwidth of such a filter depends on many factors, such as the coupling strength between the waveguides, the loss in the ARROW (diffraction, scattering, etc.), and the properties of the ARROW core layer (index and thickness). The last parameter can be more easily controlled than the other two under the current experimental arrangement. In Figure 4-2, the propagation characteristics of ARROWs with different core thicknesses are plotted. In this experiment, a 3.887µm $Al_{0.33}Ga_{0.67}$As core layer was chosen. $Al_{0.33}Ga_{0.67}$As was used because its absorption onset wavelength is well below the operating wavelength of 830nm. The thickness was chosen to minimize the bandwidth, while keeping
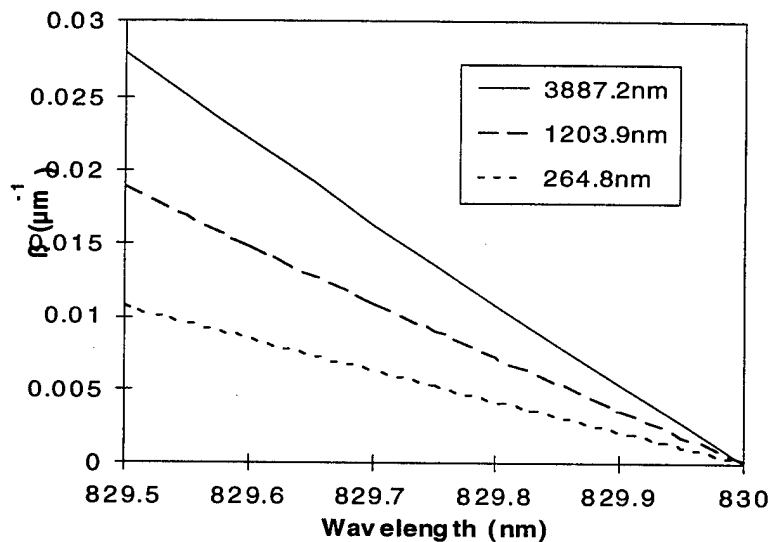

Figure 4-2. The calculated difference in propagation constants (units:1/µm) between the fiber mode and the highest order confined TE mode of the ARROW. The three curves represent three ARROWs with different core ($Al_{0.33}Ga_{0.67}$As) thicknesses.

the MBE growth time under a reasonable limit. The ARROW was designed using the transfer matrix approach. The calculated dispersion curves for the ARROW are shown in Figure 4-3, showing phasematching at 818nm (TM) and 830nm (TE).

During testing, a fiber half coupler (Canadian Instruments Ltd.) was mounted on an x-y-z stage and positioned on top of the ARROW sample. Drops of index matching fluid (n=1.458), whose index was closely matched to that of the fiber cladding (n=1.452), were applied between the fiber block and the ARROW to ensure good optical contact. The optical source used was a fiber coupled 830nm laser diode biased just below threshold. A polarizer and a fiber polarization controller were used at the input end. The experimental transmission spectra of the system were measured with a HP70951A optical spectrum analyzer and shown in Figure 4-4. The TE dip has a FWHM of 0.5nm and the TM dip has a FWHM of 1.3nm. The TM dip is broader because the DBR is less reflective for the TM mode. The positions of the dips are shifted from the design wavelength due to thickness variations in MBE growth. The insertion loss (~2.5dB) of the system is due to imperfect fiber splicing.
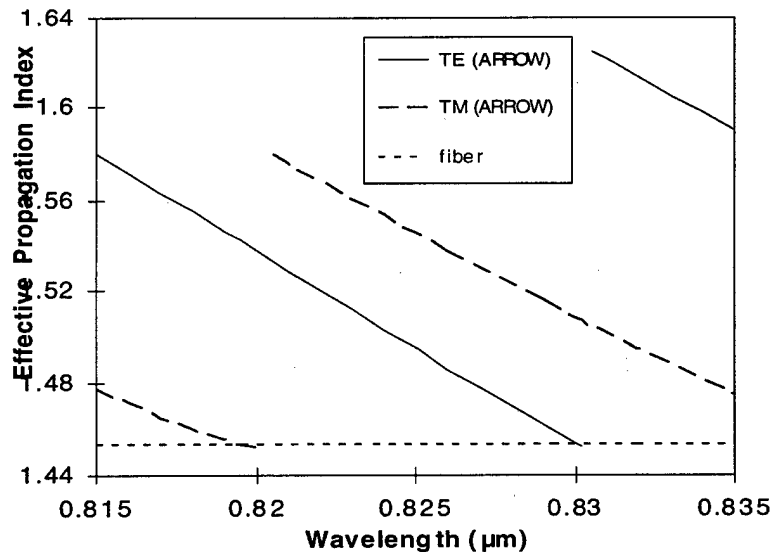

Figure 4-3. The calculated effective propagation indices for the single mode fiber and the highest order confined modes of the ARROW.
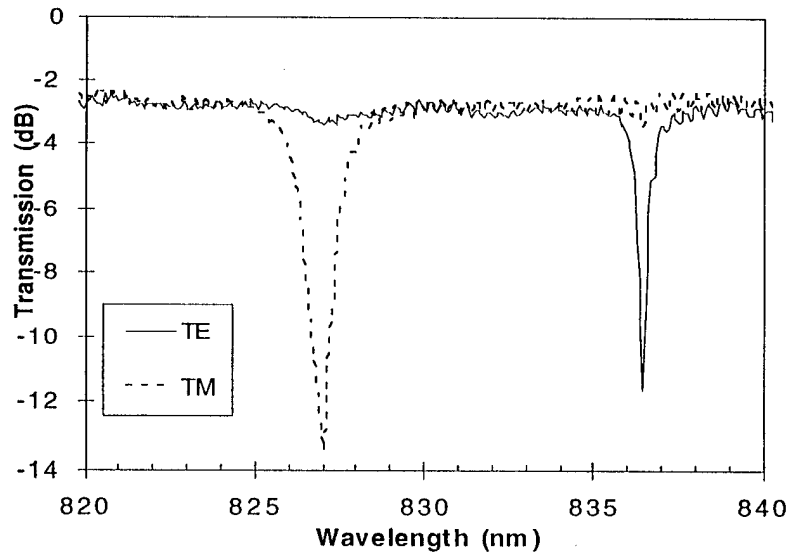
38

Figure 4-4. The measured transmission spectra of the filter (units: dB).

4.2. Conclusions

We described the concept and the implementation of a GaAs/AlGaAs in-line fiber filter suitable for WDM applications. For TE polarization, it has a bandwidth of 0.5nm and a rejection ratio of 9dB. This in-line device architecture can be extended to other active and passive devices, such as modulators and light emitters, simply by adding quantum well layers to the waveguide core.

Participating Scientific Personnel

J. S. Powell

Ph.D., Stanford University, September 1997

"Systems Applications of Vertical Cavity Multi-Quantum Well Optoelectronic Modulators"

C. W. Coldren

Ph.D., Stanford University, 2000

"Indium Gallium Nitride Arsenide Vertical Cavity Surface Emitting Laser for Optical Communication"

Inventions

None